Quartz rheology constrained from constant-load experiments: Consequences for the strength of the continental crust

Subhajit Ghosh[a]*, Holger Stünitz [a,b], Hugues Raimbourg[a], Jacques Précigout [a]

[a] *Institut des Sciences de La Terre d'Orléans (ISTO), Université d'Orléans, CNRS, BRGM, UMR7327, 45071, Orléans, France*

[b]*Department of Geology, University of Tromsø, Dramsveien 201, 9037, Tromsø, Norway*

* Corresponding author: subhajit.ghosh@univ-orleans.fr (S. Ghosh)

Abstract

The mechanical properties of quartz are fundamental to control the plastic behaviour of the continental crust. Our understanding of quartz rheology is still limited in the following respects: i) the large variability of flow law parameters in the earlier literature (stress exponent n = 4 to ≤ 2 and activation energy Q = 120 to 242 kJ/mol), and ii) the difficulty to identify the rate-limiting deformation mechanism, if several mechanisms are operating simultaneously. These two issues are connected and cannot be resolved separately. The present study has carried out constant-load experiments to constrain the flow law parameters of quartz. A new generation hydraulically-driven Griggs-type apparatus has been employed, resulting in reproducible mechanical data, even at very low strain rates (10^{-8} to10^{-9} s^{-1}; so far, closest to the natural ones). Furthermore, the Q-value in constant load experiments can be estimated without prior knowledge of the n value. Our new n (= 2) and Q values (= 110 kJ/mol) are fairly low. We calculated an A-value of 1.56 × 10^{-9} /MPa/sec. Microstructural analysis suggests that the bulk sample strain in our experiments is achieved by crystal plasticity, i.e., dislocation glide with minor recovery by sub-grain rotation, accompanied by grain boundary migration. Micro-cracking helps to nucleate new grains. It is inferred that strain incompatibilities induced by dislocation glide are accommodated by grain boundary processes, including dissolution-precipitation creep and grain boundary sliding. These grain boundary processes are responsible for the n-value that is lower than expected for dislocation creep ($n \geq 3$). The new flow law can consistently estimate strain rates (especially at low stresses) in excellent agreement with documented natural case studies and predicts a rapid drop in strength of quartz-bearing rocks in the continental crust below a depth of ~10 km or at a temperature of ~300°C and higher.

keywords: Quartz, Rheology, Flow law, Dislocation creep, Dissolution and precipitation, Dislocation Glide

1. Introduction

Quartz is one of the most important rock-forming minerals of the lithosphere. Due to its abundance, quartz rheology (i.e., polycrystalline quartz aggregate) in the presence of water forms the basis for constructing crustal strength profiles that are crucial for constraining plate tectonic processes and modelling the long-term flow behaviour of the continental crust (e.g., Kohlstedt et al., 1995). Therefore, several experimental studies in the last four decades (e.g., K&T84 ~ Kronenberg and Tullis, 1984; Koch et al.,1989; P&L90 ~ Paterson and Luan, 1990; L&P92 ~ Luan and Paterson, 1992; G&T95 ~ Gleason and Tullis, 1995; Hirth et al., 2001; S&T03 ~ Stipp and Tullis, 2003; Stipp et al., 2006; R&B04 ~ Rutter and Brodie, 2004; Kidder et al., 2016; Fukuda et al., 2018) focused on establishing a creep flow law of polycrystalline quartz aggregate (e.g., natural and synthetic quartzites, powders of natural single crystals and sand) based on the following equation:

$$\dot{\varepsilon} = A\left(\frac{\sigma^n}{d^p}\right)\exp\left(-\frac{Q}{RT}\right) \qquad (1),$$

where, $\dot{\varepsilon}$ is the strain rate, A is dimensionless constant, Q is the activation energy, R is the gas constant, T is absolute temperature, σ is the differential stress, d is the grain size, n is stress exponent and p is the grain size exponent. Theoretical models of creep have shown different values of n and p for different creep mechanisms. For example, $n = 1$ and $p = 2$ or 3 indicate lattice diffusion (Nabarro-Herring) creep (Nabbaro, 1948; Herring, 1950) or grain boundary diffusion (Coble) creep (Coble, 1963), respectively. Conversely, $n \geq 3$ and $p = 0$ generally correspond to the GSI dislocation creep process. In addition, Kohlstedt et al., (1995) introduced a water fugacity term (f_{H_2O}) in the equation (1) to account for the effect of H_2O on the creep rates at a certain pressure-temperature (P-T) condition. Accordingly, the equation (1) for the dislocation creep can be written as follows, where r is water fugacity exponent:

$$\dot{\varepsilon} = A\sigma^n f_{H_2O}^r \exp\left(-\frac{Q}{RT}\right) \qquad (2).$$

Earlier experimentally determined creep law parameters of polycrystalline quartz by different groups show many discrepancies (Table 1) that result in significant variations of predicted crustal strengths (Kohlstedt et al., 1995; Stipp et al., 2002b). The n-value vary from 4 to < 2, while the Q value vary from 120 to 242 kJ/mol, in addition to large differences in the A-value. Due to the power-law nature of equation (2), minor changes in flow law parameters can lead to significant differences in the predicted crustal strength when extrapolated to geological conditions (Hirth et al., 2001; Lusk et al., 2021; Tokle et al., 2019). In several cases the frequently used experimentally-derived flow laws can overestimate the strength of a particular region. For example, Boutonnet et al., (2013) showed that the $\dot{\varepsilon}$ calculated by any of the earlier flow laws from stresses derived from S&T03 piezometer (without the Holyoke and Kronenberg, 2010 correction) are slower than the well-constrained natural rates in the Ailao Shan–Red River (ASRR) strike-slip shear zone.

The starting material for experiments varied considerably among the earlier studies (e.g., novaculite, different varieties of quartzites, single-crystal or quartz powder to synthetic silica gel/acid), and the initial grain sizes showed more than one order of magnitude difference (Table 1). The finest grain size samples are expected to show a contribution of grain size sensitive (GSS) diffusion creep as is found in polycrystalline mineral aggregates of olivine, or clinopyroxene (Yabe et al., 2020; Ghosh et al., 2021). Importantly, different interpretations for the grain-scale deformation mechanisms, from climb-controlled dislocation creep to a combination of dislocation and diffusion creep for quartz were postulated among different studies (G&T95; Richter et al., 2018; Fukuda et al., 2018; Nègre et al., 2021). In other words, it still remains difficult to constrain the intra- and inter-grain processes responsible for plastic deformation and related flow law parameters.

In order to constrain a robust flow law for wet quartzite, we have generated novel high-resolution data through constant-load experiments at high pressure and high temperature. We used a new generation Griggs-type apparatus with natural coarse-grained (~200 μm) polycrystalline Tana quartzite (Fig. 1) to perform mechanical testing by load-stepping. This method has two main advantages compared to strain rate ($\dot{\varepsilon}$) stepping tests: (i) The equilibrium between load, $\dot{\varepsilon}$, and microstructure is achieved faster (Kohlstedt, personal communication), and (ii) The Q-value can be determined without previous knowledge of the n-value. The second point is particularly important for the extrapolation of laboratory data to lower temperature conditions in naturally deformed rocks. The wide range of Q-values in the existing literature have triggered the work by Lu and Jiang, (2019), which attributed such variations to an effect of confining pressure. Another advantage of load-stepping is that the bulk strain of the sample is smaller than in $\dot{\varepsilon}$-stepping tests, so that geometrical problems due to change in the

sample shape are minimized. We compare our results with $\dot{\varepsilon}$-stepping experiments using the same Tana quartzite to understand the effect of much larger final strain, hence, significant recrystallization (Pongrac et al., 2022). A comparison between our newly established flow law with previous results provides the opportunity to further explore the effects of using different apparatuses, choice of the sample, and the deformation mechanism on the mechanical properties of wet quartzite. Finally, we will discuss the implication of our flow law on crustal strength.

2. Methodology

2.1. Deformation tests

Load-stepping experiments during coaxial shortening were performed on natural quartzite samples in a new generation Griggs-type solid-medium (NaCl) apparatus (Fig. 2a) at ISTO (Orléans, France, Précigout et al., 2018). Cylindrical samples of 8 mm diameter were core-drilled from the starting material and dried at 110° C for one day. $\dot{\varepsilon}$ and σ for each step were obtained from the steady-state portion of the mechanical curves (see supplementary text S1).

The hit point (Fig. 2b) in the solid-medium apparatus is a major source of error in stress measurements (Holyoke and Kronenberg, 2010). When stopping the displacement of the deformation actuator, the load can decrease below the hit point (supplementary text S1). In order to account properly for such a load decrease (affecting the stress at slow displacement rates), the displacement was stopped overnight after the hit point and before the first load increment. This decrease is labelled as 'relaxation' in Figures S1 and S2. The stress correction by Holyoke and Kronenberg (2010) was not applied to the data, because the use of solid medium salt involves a subtraction of 48 MPa, resulting in zero or negative $\Delta\sigma$ values for some of our low stress experiments. We also estimated the magnitude of the axial stresses related to different displacement rates of the σ_1 piston (during our load-stepping) due to viscous drag and/or friction with the confining medium (see supplementary text for details). These values are two orders of magnitude lower than the error estimated for the hit point construction, and therefore, inconsequential for our mechanical analysis.

2.2. Starting material and sample characterization

As the starting material, we used a pure (>99% silica), natural quartzite without evidence of prior micro-scale deformation (Fig. 1) from the ELKEM quarry in Austertana (Northern Norway). The mean grain size is ~200 μm and the H_2O has been measured as of the order of ~1700 H/10^6 Si for grain interiors and ~2100 H/10^6 Si for grain boundaries in a previous study (Nègre et al., 2021). Further details on chemical and microstructural characterizations of the starting material can be found in Nègre et al., (2021) and Pongrac et al., (2022). Deformed samples were cut through the centre, parallel to the compression direction, and then characterized using Polarized light microscopy (LM), SEM-cathodoluminescence (CL) and Electron backscatter diffraction (EBSD) (see supplementary text S1).

3. Experimental results

3.1. Mechanical data

In Figure 2b and 2c, we provide a typical stepped-load test (with 0.1 wt. % of H_2O added) at a constant temperature of 900°C and a confining pressure of 1 GPa. As expected, strain increases faster per time with increasing load on the sample. We see a rapid change in strain measurements during the rapid change in the applied σ (i.e., load/area) from one stress-step to another. The slopes of the strain-time curves need some period of time to attain a steady state condition (Fig. S1). We only use the last part of the strain-time curve, where steady-state has been achieved. In our load-stepping experiments,

we have used the conventional hit point as well as the lowest point after relaxation and have carried out the mechanical data analysis with both values as hit point (Figs. S1-S2, 2d). There is no systematic effect on the *n* or *Q*-values.

The curves in figure S1 show similar characteristics for both as-is and H_2O-added experiments, although the as-is sample is ~$2-5$ times stronger than the H_2O-added sample at 900°C (Fig. 3a). Depending on the number of steps and $\dot{\varepsilon}$ at each step, the bulk strain in our experiments ranges up to a maximum value of ~16%. Experimental conditions and results from each stress-step from corresponding experiments are sequentially shown in Table 2. During the as-is experiment (OR90), we repeated the lowest stress-steps acquired during increasing (39.59 and 67.89 MPa) and then during decreasing load (61.50 and 29.22 MPa) to identify the effect of time and microstructural evolution during the experimental run time. The 67.89 and 61.50 MPa steps show similar creep rates, which are within the error generally given for the Griggs-type instruments (Holyoke and Kronenberg, 2010). However, for the lowest stress-steps (29.22 and 39.59) the difference in $\dot{\varepsilon}$ is relatively substantial (4.6 times) compared to the difference of σ (1.35 times).

In addition to load-stepping experiments, we have performed three *T*-stepping experiments at constant load: two with 0.1 wt. % H_2O added and one as-is (Table 2b). The mechanical data for the two H_2O-added experiments are identical, even the slope of the individual stress-steps have similar patterns (Figs. 2d, S2). At the highest *T*-step, the overall slope of the strain curve is slightly convex, while it becomes slightly concave at the lowest *T*. The σ values also decreased slightly (~10MPa) with time as a consequence of the increase in the surface area of the deformed sample (as the load is constant). We used the hit point after relaxing overnight to calculate the *Q*-value. Noticeably, all the data points for the OR94 with lower stress-values are ~0.76 times faster than the OR97 with slightly higher stress-values, under the exact same condition of deformation (Table 2). Such minor differences in σ and $\dot{\varepsilon}$ values are likely to be related to the inherent mechanical error, for example, in constraining the hit point. In addition, the oil pressure in the hydraulic-rams is temperature-sensitive, and some variation may be related to small room temperature variations during deformation.

3.2. Determination of *n* and *Q*

σ and $\dot{\varepsilon}$ for all the experiments were plotted in a log-log diagram to calculate the *n*-value (Fig. 3). The slope of the global-fit indicates a *n*-value of ~1.7 for H_2O-added and ~1.85 for the as-is sample (Fig. 3a). We noticed that the lowest stress points (55.90, 39.83 and 39.59 MPa) measured at the beginning of the load-stepping experiments exert a strong control on the overall global fit. If we do not consider these lowest stress data points, then all the global-fits approach $n \approx 2$ (Figs. 3b, c). A recent communication (Pongrac et al., 2022) has reported $n \approx 2$ from co-axial $\dot{\varepsilon}$-stepping experiments using the same Tana quartzite. These experiments (plotted as PP in Fig. 3b) were performed in a conventional Griggs apparatus located at the University of Tromsø. The samples deformed in Orléans are slightly stronger than samples deformed in Tromsø under the same P-T conditions (Fig. 3b, c).

We plot all of our temperature-stepping data in the Arrhenius $ln(\dot{\varepsilon}) - T^{-1}$ space (Fig. 4). To calculate the *Q*, we used the equation (2) in the following form.

$$ln(\dot{\varepsilon}) = -\left(\frac{10^4}{\mathrm{T}} \times \frac{\mathrm{Q}}{10^4 \mathrm{R}}\right) + ln\left(A f_{H_2O}^{r} \sigma^{n}\right) \quad (3)$$

In this way, the *Q*-value can be calculated independently of the *n*-value. The similar slope of the global-fit for both H_2O-added experiments can be well fitted with a single Arrhenius equation with similar values of activation energy (i.e., *Q* = 110 kJ/mol) (Fig. 4a). In order to make sure whether the choice of hit point can affect the *Q*-value or not, we have calculated *Q* using the conventional hit point, too (Fig.

S2). There is no difference in the result. But the *Q* is slightly (~5 kJ/mol) lower for the as-is sample (Fig. 4b). Considering the inherent errors associated with Griggs-type apparatuses, such minor differences are not significant. Therefore, we consider the *Q*-value as the same for the H_2O-added and as-is samples.

3.3. Microstructural observations and interpretations

CL-imaging of the undeformed Tana quartzite shows that the individual quartz grains are composed of cores of rounded detrital quartz grains with various colours and intensity, surrounded by a dark authigenic SiO_2 cement (Fig. 5a). The cement is in crystallographic continuity with the sand grains on which it grows expitaxially (Fig. 1). Due to the filling of the pore space by authigenic SiO_2 cement, no visible porosity was detected by the LM or SEM. Detailed microstructural characterizations and H_2O content of the deformed (Tana) samples have been presented in two earlier studies (Nègre et al., 2021; Pongrac et al., 2022). Therefore, in the present contribution, we will only summarize the microstructural observations and put the observed grain-scale deformation mechanism into context with our new flow law data.

Under the LM, both, the as-is and H_2O-added samples show evidence of crystal-plastic deformation features, such as undulatory extinction, deformation lamellae, and sub-grains. We can observe some intragranular micro-cracking (Fig. 5c), unrelated to the unloading cracks. Furthermore, a new material with a bright luminescence appears surrounding original quartz grains and in the cracked regions (Figs. 5d-h), indicating the operation of dissolution-precipitation creep (DPC) processes in the presence of fluid. Fluid migration along the grain boundaries and cracks makes them visible in CL-images. Cracked regions typically form along the boundaries of quartz grains (Figs. 5g, h, 6a). Larger, CL-dark fragments can be seen within lighter luminescent material, preserving their angular shape (Fig. 5f, 6a). We notice that these zones are sometimes associated with porosity development (Fig. 5e). In addition, we can identify mode-I cracks (marked by yellow arrow) parallel to the compression direction (Figs. 5e). Such 'axial splitting' cracks typically form at low confining pressures, most likely early in the experimental procedure, before attaining the deformation conditions (Pongrac et al., 2022). These mode-I cracks are volumetrically small (<1%) and discrete. Typically, all cracks lack any offset. As a result, these cracks hardly accommodate any strain and should not have a substantial effect on the bulk strength of the samples. Lobate grain boundaries, indicative of grain boundary migration (GBM) is also associated with the appearance of the bright luminescence (Fig. 5h).

EBSD mapping reveals some degree of crystal plasticity in the original quartz grains, giving rise to the development of low-angle boundaries (Figs. 6b, c). Such low-angle inner boundaries (marked in yellow) correspond to grains with intense patchy undulatory extinction under the LM. The distorted crystal structures can develop into discrete sub-grain boundaries (red lines) (Fig. 6b). Most of these low-angle boundaries are typically found near the grain boundary regions (Fig. 6b). A few of these low-angle boundaries correspond to micro-cracks in the CL image (Fig. 6a). A comparison between sub-grain boundaries along with the IPF colour map (Fig. 6c) indicates the formation of incipient recrystallized grains along grain boundaries by progressive sub-grain rotation. We report a mean recrystallized grain-size of 6.23 µm, following our EBSD data treatment (see supplementary for procedure). Misorientation axes distribution of low-angle boundaries (sub-grains) suggests that prism <a> slip is statistically dominant with subordinate rhomb <a> slip (Fig. 6e). In addition to sub-grain rotation, a portion of such new grains were originated by micro-cracking (Fig. 5c). The new grains developed by cracking are identified by their bright luminescence and the associated porosity development.

4. Discussion

4.1. Constitutive equation

We found that the values of n = 1.7 or 2 and Q = 110 kJ/mol represent our wet and as-is quartzite mechanical data well (Figs. 2, 3). As mentioned above, the low-stress data (e.g., 39.59 MPa for the as-is experiment in Table 2a) measured at the beginning of the stress-stepping experiments exerts a strong control on the slope of the global-fit that indicates $n < 2$. Such low flow stress regimes with $\dot{\varepsilon}$ on the order of 10^{-8}–10^{-9} s^{-1} have not been achieved earlier with coarse-grained quartzite (Table 2a). A few studies like the ones of S&T03, R&B04, and Richter et al. (2018) reported low flow stresses of 30 to 66 MPa, but the associated $\dot{\varepsilon}$ are on the order of 10^{-7} to 10^{-6} s^{-1}. For the as-is experiment, we repeated the step at low stress (i.e., 29 MPa), after conducting several steps at higher stresses. Interestingly, this data point conforms with the $n \approx 2$ global-fit. A ±30 MPa error is generally associated with traditional Griggs-type apparatus that may influence the precision of the low-stress data. Jaoul et al., (1984), also discarded the first lowest-stress increment data from their load-stepping experiments because of lower accuracy.

Using the equation (2), the pre-exponential term (A) is calculated for all the T-steps from H_2O-added samples, reported in table 2b, considering n = 2 and $f_{H_2O}^{r}$. The f_{H_2O} is calculated for a known P-T (Tony Wither's fugacity calculator), assuming an a_{H_2O} of 1 and the water fugacity exponent (r) of 1 (Kohlstedt et al., 1995; Fukuda et al., 2018). Thereafter, we take the average of those A-values, which is 1.56 × 10^{-9} /MPa/sec. The A-value for the as-is sample will be 2-4 times lower. The modified flow law for the 0.1 wt.% H_2O-added quartzite is as follows:

$$\dot{\varepsilon} = 1.56 \times 10^{-9}\ _{/\mathrm{MPa/sec}} \cdot \sigma^{2} \cdot f_{H_2O} \cdot \exp\left(-\frac{110\ \mathrm{kJ/mol}}{\mathrm{R}T}\right) \quad (4).$$

Négre et al., (2021) showed that the water fugacity exponent, r can be 0.92 for n = 2. In that case, the A-value in our flow law will be 2.83 × 10^{-9} /MPa/sec.

4.2. Comparison with previous studies: non-dimensional plots

After establishing the constitutive equation for the Tana quartzite, we can use it as a reference to compare the original mechanical data from experiments reported in the literature. For this purpose, we normalized all the original mechanical data (σ and $\dot{\varepsilon}$) to non-dimensional stress (σ_0) and strain rate ($\dot{\varepsilon}_0$) ratios:

$$\sigma_0 = \frac{\sigma}{\sigma^{*\mathrm{ref}}} \text{ and } \dot{\varepsilon}_0 = \frac{\dot{\varepsilon}}{\dot{\varepsilon}^{*\mathrm{ref}}} \quad (5).$$

Here, the reference strain rate ($\dot{\varepsilon}^{*\mathrm{ref}}$) is calculated from our new wet-quartzite flow law (Eq. 4) by substituting the T with temperature-values, f_{H_2O} with those values at which each original mechanical data was acquired and the stress-term (σ) with the $\sigma^{*\mathrm{ref}}$. We used a fixed value of 100 MPa as $\sigma^{*\mathrm{ref}}$ in this calculation.

In order to compare the effect of temperature on the creep rates with those given in the existing literature, we created an Arrhenius space of non-dimensional strain rate ($\dot{\varepsilon}_0$) and the inverse of temperature (T_0^{-1}):

$$\dot{\varepsilon}_0 = \frac{\dot{\varepsilon}}{\dot{\varepsilon}^{*\mathrm{ref}}} \text{ and } \frac{10000}{T_0} = \frac{10000}{T} - \frac{10000}{T^{*\mathrm{ref}}} \quad (6).$$

Here, the reference strain rate ($\dot{\varepsilon}^{*\mathrm{ref}}$) is calculated from our flow law (Eq. 4) by substituting the stress-term (σ) with original reported σ-values and the temperature (T) is substituted by $T^{*\mathrm{ref}}$. We used a fixed value of 1173 K as $T^{*\mathrm{ref}}$. The f_{H_2O} is calculated for the $T^{*\mathrm{ref}}$ and the pressure at which each original mechanical data was acquired. It should be noticed that T_0^{-1} is not a dimensionless ratio in this plot. Previously, the non-dimensional plots were used in comparing mechanical data of olivine and

diopside (Yabe et al., 2020; Ghosh et al., 2021). This method differs from using reported flow law parameters to compare results among different studies, where mechanical data were obtained from different stresses, strain rates, temperatures and pressures. To make a rational comparison with our experimental condition, we only included the results from studies that were conducted in a coaxial geometry at ≥750°C, and that satisfy the Goetze's criterion ($\Delta\sigma \leq P_{conf}$).

Our wet-quartzite creep data are transformed to σ_0, $\dot{\varepsilon}_0$ and T_0^{-1} plots along the reference line (corresponding to the slope of the stress exponent and the activation energy, respectively) in figure 7, which confirms the capability of equation (5) and (6) to express our original mechanical data in a predicted manner. In this way, we are able to compare the mechanical data from the earlier studies to our creep data. All the data show a power-law relationship in a non-dimensional $\sigma_0 - \dot{\varepsilon}_0$ space (Fig. 7a). Clearly, creep results obtained from natural coarse-grained (~100-200 μm) quartzites broadly overlap with or follow our data. Even the absolute strengths are essentially comparable (within a factor of ~5 times the $\dot{\varepsilon}$, indicated by the shaded region in Figure 7a), considering a ±30 MPa accuracy of the conventional solid-medium apparatus (Holyoke and Kronenberg, 2010). Most of the fine-grained (~10-20 μm) samples from Fukuda et al., (2018), R&B04, and synthetic samples from L&P92 are weaker compared to the coarse-grained natural samples (except coarse silica gel samples of L&P92). Similar observations are also made for the $\dot{\varepsilon}_0 - T_0^{-1}$ plot in the Arrhenius space (Fig. 7b), where data obtained using natural quartzite overlap with our results. The overlap indicates a comparable effect of temperature on the $\dot{\varepsilon}$ and shows that our low *Q*-value (110 kJ/mol; Table 1) is consistent with results of K&T84, Koch et al., (1989), and P&L90. It is surprising to find a lower temperature dependency (similar to our data) for the melt-free samples of G&T95, although they reported a higher *Q*-value of 223 kJ/mol. Their melt-present samples indicate an even lower slope for a reported *Q*-value of 137 kJ/mol (Fig. 7b).

On average the strength of the as-is Tana sample is higher than the 0.1 wt.% H_2O-added ones (Fig. 7a). This situation is also observed in earlier studies (K&T84; Jaoul et al., 1984). Interestingly, the as-is (G&T95; S&T03) and 0.2 wt.% H_2O-added (Stipp et al., 2006) data using the Black hills quartzite do not show such discernible effect of H_2O on the $\dot{\varepsilon}$ with increasing temperature (Fig. 7a). The common thread between these latter studies is that they were performed in a molten-salt-assembly and contrasts with Black hills quartzite data from deformation experiments in a solid-medium apparatus (Kidder et al., 2016). At a lower P-T (900°C, 1.3 GPa) they plot closely to the above-mentioned studies, possibly due to the retention of added H_2O (0.2% wt.%). Diffusion of H_2O from quartz is very slow at an experimental time-scale (Kronenberg et al., 1986; Gerretsen et al. 1989), but H_2O can still be transferred between the grains and grain boundary regions by microcracking. Additionally, the molten salt shows a complete solid solution with H_2O above 150 MPa pressure (Bodnar et al., 1985), so that the melt in the confining medium is not buffered for H_2O. Given the ease of hydrogen-diffusion through the Pt jacket, it is possible that H_2O is effectively lost from the samples in molten salt assemblies at high temperature. Indeed, even a minor amount of melt (present in G&T95) along the grain boundaries might preferentially attract water, and dry the primary grains (Jaoul et al., 1984). The H_2O content measured by Stipp et al., (2006) from deformed as-is and vacuum-dried specimens show an overall decreasing trend with increasing temperature that may support the conclusion of a drying effect of the molten-salt-assembly. This conclusion may appear inconsistent if several data points from molten-salt-medium experiments are compared with our Tana quartzite data, yielding slightly weaker or overlapping results. However, considering the differences between the apparatus, experimental conditions (e.g., confining pressure), initial sample composition (e.g., the water and impurity content), and normalization method incorporating fugacity estimations, it is apparent that the bulk strengths of those samples are not much different from our results. It emerges from the systematic strength

difference that we observe between the 'H_2O-added' and 'as-is' Tana samples that it is more reasonable to compare the results of as-is and H_2O-added samples only from molten-salt experiments conducted at the same condition (i.e., 1.5 GPa) in the same apparatus.

It is noteworthy that the earlier $\dot{\varepsilon}$-stepping experiments (e.g., Négre et al., 2021, Pongrac et al., 2022) required higher strain to achieve steady-state conditions. Yet, we can express all the previously obtained experimental results from different groups using coarse-grained natural quartzites based on similar $\dot{\varepsilon}$ dependencies on σ and T as our mechanical data. More significantly, it seems that a larger amount of strain, which should result in more recrystallized material (including different regimes in Hirth and Tullis, 1992) in the earlier studies does not have a great effect on the overall strength of the material, although this needs to be tested in future studies. These observations are indicative of the operation of the same underlying rate-limiting creep mechanism irrespective of the degree of recrystallization (at least in the order at which these studies were conducted). Furthermore, the same *n*-values at considerably high total strain in Pongrac et al., (2022) indicate that our *n*-values at lower strain are not the result of transient creep.

Contrarily, a number of data from fine-grained samples (especially L&P92; R&B04) are significantly weaker than coarse-grained samples in our non-dimensional plot, indicating some additional effect due to fine grain size. The *T*-stepping data of Fukuda et al., (2018) show a steeper slope (Fig. 7b), indicative of a higher *Q*-value, as originally reported. Fukuda et al., (2018) and Richter et al., (2018) recognized a mixed mode of deformation mechanism for their fine-grained samples that includes the contribution of diffusion and/or grain boundary sliding (GBS) and dislocation creep. Following their comprehensive study, it is also reasonable to assume the same for the fine-grained powder of R&B04 and silica acid originated samples of L&P92. Although the silica-gel-originated samples show a larger grain size (90 μm), a contribution from grain boundary processes was also interpreted due to the presence of impurities at the grain boundaries (L&P92).

4.2.1. Interpreting higher *n*-values from earlier literature

Recently, Tokle et al., (2019) and Lusk et al., (2021) compiled and reviewed earlier experimental studies in order to obtain usable flow parameters. They proposed two distinct correlations with the experimental conditions at which those studies were performed. According to Tokle et al., (2019), the higher *n*-values correspond to the lower differential stresses and the lower *n*-value to higher stresses, and both can be linked to activated slip systems. However, in this way they are essentially treating all the earlier studies, utilizing different techniques, apparatus, and materials for experiments in the same way. On the other hand, Lusk et al., (2021) implied that low confining pressures (< 0.56GPa) resulted in higher *n*-values and higher pressures (0.7–1.6 GPa) in lower ones. As noted by the authors, the low confining pressure conditions are restricted to Paterson-type gas medium apparatus (Table 1), in contrast to Griggs-type apparatus for high confining pressure experiments. The G&T95 study at ~1.5 GPa confining pressure and n = 4, using a molten-salt-assembly in the Griggs-type apparatus is an exception in this trend. Moreover, at high confining pressure (1 GPa), Fukuda et al., (2018) showed that the *n*-value determined at low temperature (600 – 750°C) and higher stress range is substantially higher (2.9 to 5.2) for fine-grained quartz, indicating power law breakdown (Richter et al. 2018). A careful inspection reveals that the lower *n*-value studies can be connected with high-confining pressure ones, but exclusively using solid-salt-assemblies (Table 1). More complication can arise from the fact that any theoretical and statistical re-analysis (Fukuda and Shimizu, 2017; Tokle et al., 2019; Lusk et al., 2021) of earlier experimental studies results in a substantially different flow law parameters from what is originally reported (see supplementary text S2, S3). Therefore, a re-evaluation of the wet quartzite

GSI flow law for coarse-grained polycrystalline aggregates, considering the above-mentioned contradictions, is needed.

We tried to verify the n = 4 from G&T95 by plotting their reported creep data in the $\log \sigma - \log \dot{\varepsilon}$ space, but the n-value came down to ~3.6 (Fig. S3a). In the original study, the authors did not include the highest stress points, assuming a different deformation mechanism was active at the higher stress condition. Nonetheless, their result has not been reproduced by any subsequent as-is or H_2O-added studies. Interestingly, the high n-value is similar to the vacuum-dried natural quartzites from solid-medium apparatus (Table 1; K&T84; Jaoul et al., 1984). As mentioned in the above section, in our non-dimensional space (negating the effect of temperature) (Fig. 7a), the molten-salt-medium experiments with a given material (i.e., Black hills quartzite), show no effect of added H_2O. We suspect that the molten-salt-assembly might effectively dry the sample during the experiment, causing a similar strength between the as-is and H_2O-added samples. As interpreted in Jaoul et al., (1984), the high n-values (> 3) in these dried samples were caused by the transition to brittle behaviour leading to power law breakdown (*cf.* Richter et al., 2018). A similar explanation for the increase in the n-value from 1.7 to 5 is given for the fine-grained samples from Fukuda et al., (2018) deformed under high stress and low-temperature conditions (*cf.* Richter et al., 2018).

The values of $n \approx 3$ from fine-grained wet-samples deformed under high-T condition in a Paterson apparatus are difficult to interpret as compared to Fukuda et al., (2018) with n = 1.7 (Table 1). The driest sample (i.e., crushed fine-grained Brazilian single-crystal quartz with added H_2O) that has been deformed by R&B04 to construct a 'wet' quartzite flow law has reported n = 2.97. Using the same type of gas apparatus, the $\dot{\varepsilon}$-stepping data from the synthetic silica-acid-derived polycrystalline quartz of L&P92 produces a value of n = 4 (modified to 3 by Fukuda and Shimizu 2017) without considering the Goetze's criterion. According to this criterion, the σ_1 higher than the confining pressure results in partly brittle deformation, even in high T. Noticeably, the L&P92 flow law cannot predict its original creep data (Fig. S8). A steeper slope is observed for the Paterson experiments in our non-dimensional comparison (Fig. 7a). The combination of low confining pressure and the drying effect of the argon gas as the confining medium (similar to the molten-salt-assembly) in the Paterson apparatus may lead to partial brittle behaviour (Kohlstedt et al., 1995) that could explain the high n-value for these fine-grained samples (*cf.* Richter et al., 2018). A few data from Paterson experiments (R&B 2004) at the lowest stress condition plots very close to our results. This observation supports our interpretation that with increasing stress the deformation will transition to a brittle behaviour under low confining pressure.

In summary, we interpret that a $n \geq 3$ for coarse-grained (from molten-salt-medium and 'vacuum-dried' samples of solid-medium) and fine-grained quartzite (from gas-medium and solid-medium apparatus), resulted from the onset of brittle mechanisms. The $n \leq 2$ for coarse-grained (this study) and fine-grained (9.5-12 μm; Fukuda et al., 2018) quartzites resulted from power-law deformation due to retention of water under the high confining pressure (satisfying Goetze's criterion) in solid-medium Griggs apparatus.

4.3. Deformation mechanism of wet quartzite

Commonly climb-controlled dislocation creep is inferred for the plastic deformation of quartz, requiring a theoretically expected n-value of 3-5 (Karato 2008, Paterson 2012). A n-value of ≤ 2 (Table 1) requires that other processes than climb are rate-limiting for the deformation. Crystal-plastic deformation features like undulatory patchy extinction, deformation lamellae, kink bands, and minor recovery by sub-grain formation/rotation and recrystallization, limited grain boundary migration accompanied by dissolution-precipitation and micro-cracking are observed in the microstructures of our deformed samples (Figs. 5, 6). In order to explain the low n-values, a contribution of diffusion creep in

addition to dislocation creep has been inferred (Fukuda et al., 2018, Richter et al., 2018; Négre et al., 2021, Pongrac et al., 2022). However, diffusion creep mechanisms are sensitive to grain size (Herring, 1950; Nabbaro, 1948). Thus, a grain-size-dependence is expected if diffusion creep is operating together with dislocation creep, and the contribution of diffusion creep should increase with decreasing grain size. Moreover, our study reports similar *n*-values as Fukuda et al., (2018), who have used fine grained quartz powder. Additionally, the amount of recrystallization in our samples is less than ~5%, so that the grain size has remained coarse, indicating that the contribution of diffusion creep remains difficult to explain.

According to the von Mises criterion, at least five independent sets of slip systems are needed to achieve homogeneous deformation dominantly by glide mechanism in a polycrystalline material (Karato, 2008). However, the contribution from other modes of deformation mechanisms like diffusion creep and/or grain boundary sliding (GBS) can relax this condition (Hutchinson, 1977), and the deformation can be achieved by activating fewer slip systems. Such a combination of processes was inferred for wet ice (Goldsby 2006; Kuiper et al., 2020), where *n*-values of 1.8 and 2.4 are explained by the combination of basal slip (dislocation glide) and GBS (Goldsby and Kohlstedt, 2001). In that case, the strain incompatibilities and hardening from dislocation glide are accommodated by grain boundary processes without activating other harder slip systems. For GBS-accommodated basal glide only a weak or no grain size dependence is observed in ice-experiments (Goldsby 2006). Recently, Tokle et al., (2019) also suspected a GBS component in the overall deformation of quartz aggregates. However, their interpretation of dislocation accommodated grain boundary sliding (disGBS) would imply a grain size dependence, whereas the *n*-values of ~2 are observed in both, coarse (this study) and fine-grained material (Fukuda et al. 2018, Richter et al. 2018). In addition, it is evident from CL-images that DPC was active at our experimental conditions (*cf.* Nègre et al., 2021, Pongrac et al., 2022). The presence of H_2O and dissolution-precipitation may weaken the grain boundary region and promote strain accommodation by sliding along boundaries. Recently, a comparable mechanism was inferred in olivine (Samae et al., 2021), where grain boundary amorphization promotes GBS, leading to the viscosity drop in mantle rocks. In analogy to ice (and perhaps olivine), we propose that strain is achieved in coarse-grained wet quartzite by dislocation creep (mainly glide), accommodated by grain boundary processes including DPC and GBS. It has already been shown from similar experiments to ours that the bulk sample shortening is accommodated primarily (within a few percent errors) by the plastic strain of individual quartz grains (Négre et al., 2021). Consequently, DPC and GBS both appear to act as serial processes accommodating strain incompatibilities during dislocation glide where an insufficient number of slip systems operates.

Summarizing, the $n = 2$ for quartzite is attributed to a combination of dislocation glide, GBS and DPC as serial processes. The increased solubility of SiO_2 in H_2O at elevated P-T (Manning, 1994, 2018) makes the DPC mechanism very efficient at our experimental conditions and may in part explain the strength difference between our as-is and H_2O-added samples. The inverse relation of wet quartzite strength to increasing pressure may also be a consequence of increased DPC activity (Nègre et al., 2021). So far, we do not observe a grain-size-sensitivity for the operation of grain boundary processes (GBS+DPC).

4.4. Geological applications

In order to validate the laboratory flow laws, it is necessary to compare available natural data with the predicted rheology from experiments. This is commonly done by calculating strain rates ($\dot{\varepsilon}$) for given stress and temperature values. Stresses usually are obtained using recrystallized quartz grain size (d) piezometry, and deformation temperatures, usually from petrology of synkinematic mineral

assemblages. As mentioned in the introduction, sometimes the experimentally derived flow laws can underestimate the geologically reasonable $\dot{\varepsilon}$, and therefore tend to overestimate the strength of the crust (e.g., Behr and Platt, 2011; Boutonnet et al., 2013). Here, we test the validity of our wet quartzite flow law (equation 4) against three well-studied geological regions, where the geological $\dot{\varepsilon}$ can be estimated (Table 3): i) Eastern Tonale line, a mylonite zone of the Italian Alps (Stipp et al., 2002a, b); ii) Whipple fault of the Whipple Mountains metamorphic complex in eastern California (Behr and Platt, 2011); and iii) the Ailao Shan–Red River (ASRR) strike-slip shear zone in southwest China (Boutonnet et al., 2013). In all of our calculations, we used the S&T03 piezometer to calculate the σ from the d value (without any 3D correction).

The Tonale Line is a dominantly strike-slip fault that displaces rocks along the Adamello pluton, which acts as a local heat source producing a contact aureole across the fault zone. Considering a displacement of 20 to ~180 (100-150) km over 3 to 6 Ma (see Table S2), a $\dot{\varepsilon}$ range of 1.60×10^{-12} to 2.11×10^{-13} s^{-1} can be estimated for a ~1km wide fault zone. Using the d and T provided in Stipp et al., (2002b), our flow-law predicts an $\dot{\varepsilon}$ range of 1.16×10^{-12} to 1.40×10^{-13} s^{-1}. Similarly, for the extensional Whipple fault from d and T values provided by Behr and Platt, (2011) we can predict a $\dot{\varepsilon}$ range of 8.10×10^{-12} to 1.48×10^{-13} s^{-1}, where a natural $\dot{\varepsilon}$ of 1.60×10^{-11} s^{-1} was inferred by Stockli et al., (2006). A well-constrained natural $\dot{\varepsilon}$ of $3.5 \pm 0.5 \times 10^{-14}$ s^{-1} was measured from the three sets of synkinematic dikes (Sassier et al., 2009) in the ASRR fault zone. Using the d and T data from Boutonnet et al., (2013), we predict $\dot{\varepsilon} = 2.10 \times 10^{-13}$ to 2.33×10^{-13} s^{-1}. Considering the uncertainties associated with d, P, and T calculations, our new flow law predicts $\dot{\varepsilon}$ values that are in better agreement with constraints from natural observations than the previous flow laws (Table 3). In the case of the Tonale line strike slip zone, where natural constraints imply a constant P and a constant displacement rate across the zone, it is evident that our flow law provides the most consistent results irrespective of a change in T and σ. At high-T and low-σ conditions, the Hirth et al., (2001) and especially the other flow laws significantly overestimate the strength of the Tonale shear zone. On the contrary, our new flow law with $n = 2$ predicts reasonable strain rates even at low stress conditions (Table 3). These observations provide an argument against a n-value transition with increasing stress (Tokle et al., 2019).

The stress *versus* depth profile (assuming the average density of the crust as 2700 kg/m^3) predicted by our flow law shows the onset of plasticity (~ brittle to viscous transition) is expected at 9-10 km depth corresponding to ~300 °C, considering a $\dot{\varepsilon} = 10^{-12}$ s^{-1} and a geotherm of 30 °C/km (Fig. 8). This is similar to what is usually inferred from seismological observations as the down-dip limit of the seismogenic crust (e.g, Scholz, 1998). The flow law of this study shows a distinct shape of the stress *versus* depth profile in comparison to the previous studies (Fig. 8). The shape of the curves derived from previous flow laws indicate a more gradual change in strength of the crust with depth. In contrast, the flow law of this study predicts a rapid drop in strength below a depth of ~10 km (~300°C). At shallower conditions, the Hirth et al., (2001) flow law predicts a lower strength in comparison to our flow law. However, after the onset of plasticity (considering our flow law), the stress values decrease to lower strengths than the other flow laws, indicating a maximum strength of the continental crust that is restricted between 9 to 10 km and a low strength of mid- to lower continental rocks modally dominated by quartz.

5. Conclusions

Constant load experiments have yielded new flow law parameters for coarse-grained (~200 μm) wet quartzite, giving rise to a stress exponent of $n \approx 2$ and an activation energy of $Q = 110$ kJ/mol. Microstructural analysis shows that the sample strain in the wet-quartzite is achieved by grain-scale crystal-plastic processes like dislocation glide with limited recovery, accompanied by grain boundary migration and micro-cracking. Dislocation glide is the main strain producing process. Grain boundary processes, including dissolution-precipitation and grain boundary sliding are inferred to accommodate strain incompatibilities arising from the operation of insufficient slip systems. In the presence of H_2O,

the grain boundary processes (GBS + DPC) become crucial for the overall plastic deformation. We interpret that a n = 4 value (G&T95; L&P92) in the earlier literature resulted in part from the onset of brittle mechanisms, caused potentially either by drying effects of the sample (molten-salt-assembly) or lower confining pressure in a gas apparatus. In non-dimensional space, our new flow law can express the previous experimental data (performed using a Griggs apparatus) from natural coarse-grained samples (~100-200 μm) within a factor of ~5 times the strain rate. Finally, our flow law can estimate strain rates in excellent agreement with documented natural case studies and inferred natural values. In contrast to the previous studies, our flow law suggests that the strength of the continental crust is consistently lower at temperatures above ~300°C when controlled by quartz rheology.

Acknowledgements

The f_{H_2O} can be calculated from Tony Wither's fugacity calculator (https://www.esci.umn.edu/people/researchers/withe012/fugacity.htm), assuming the water pressure approximates the confining pressure during the deformation. Raw mechanical and EBSD data are available in Zenodo (10.5281/zenodo.5901073). We gratefully acknowledge the support from both LabEx VOLTAIRE (LABX-100-01) and EquipEx PLANEX (ANR-11-EQPX-0036) projects. SG acknowledged Leif Tokle for discussions. We thank G. Hirth and A. Kronenberg for their very constructive and insightful reviews that have substantially improved this manuscript. We are also thankful to J. P. Avouc for handling this manuscript.

References

Behr, W.M., Platt, J.P., 2011. A naturally constrained stress profile through the middle crust in an extensional terrane. Earth Planet. Sci. Lett. 303, 181–192. https://doi.org/10.1016/j.epsl.2010.11.044

Bodnar, R.J., Burnham, C.W., Sterner, S.M., 1985. Synthetic fluid inclusions in natural quartz. III. Determination of phase equilibrium properties in the system H2O-NaCl to 1000°C and 1500 bars. Geochim. Cosmochim. Acta 49, 1861–1873. https://doi.org/10.1016/0016-7037(85)90081-X

Boutonnet, E., Leloup, P.H., Sassier, C., Gardien, V., Ricard, Y., 2013. Ductile strain rate measurements document long-term strain localization in the continental crust. Geology 41, 819–822. https://doi.org/10.1130/G33723.1

Byerlee, J.D., 1978. Friction of rocks. Pure Appl. Geophys. 116, 615e626.

Chernak, L.J., Hirth, G., Selverstone, J., Tullis, J., 2009. Effect of aqueous and carbonic fluids on the dislocation creep strength of quartz. J. Geophys. Res.: Solid Earth 114. https://doi.org/10.1029/2008JB005884

Fukuda, J. ichi, Holyoke, C.W., Kronenberg, A.K., 2018. Deformation of Fine-Grained Quartz Aggregates by Mixed Diffusion and Dislocation Creep. J. Geophys. Res. Solid Earth 123, 4676–4696. https://doi.org/10.1029/2017JB015133

Fukuda, J.I., Shimizu, I., 2017. Theoretical derivation of flow laws for quartz dislocation creep: Comparisons with experimental creep data and extrapolation to natural conditions using water fugacity corrections. J. Geophys. Res. Solid Earth 122, 5956–5971. https://doi.org/10.1002/2016JB013798

Gerretsen, J., Paterson, M.S., McLaren, A.C., 1989. The uptake and solubility of water in quartz at elevated pressure and temperature. Physics and Chemistry of Minerals 16. https://doi.org/10.1007/BF00199553

Ghosh, S., Koizumi, S., Hiraga, T., 2021. Diffusion creep of diopside. J. Geophys. Res. Solid Earth. https://doi.org/10.1029/2020jb019855

Gleason, G.C., Tullis, J., 1995. A flow law for dislocation creep of quartz aggregates determined with the molten salt cell. Tectonophysics 247, 1–23.

Goldsby, D.L., Kohlstedt, D.L., 2001. Superplastic deformation of ice: Experimental observations. J. Geophys. Res. Solid Earth 106, 11017–11030. https://doi.org/10.1029/2000jb900336

Goldsby, D.L., 2006. Superplastic flow of ice relevant to glacier and ice- sheet mechanics. Glacier science and environmental change, pp.308-314.
Herring, C. 1950. Diffusional viscosity of a polycrystalline solid. Journal of Applied Physics, 21(5), 437–445
Heilbronner, R., Tullis, J., 2002. The effect of static annealing on microstructures and crystallographic preferred orientations of quartzites experimentally deformed in axial compression and shear. Geol. Soc. Lond. Spec. Publ. (200), 191–218. https://doi.org/10.1144/GSL.SP.2001.200.01.12
Hirth, G., Teyssier, C., Dunlap, W.J., 2001. An evaluation of quartzite flow laws based on comparisons between experimentally and naturally deformed rocks. Int. J. Earth Sci. 90, 77–87. https://doi.org/10.1007/s005310000152
Hirth, G., Tullis, J., 1992. Dislocation creep regimes in quartz aggregates. J. Struct. Geol. 14, 145–159. https://doi.org/10.1016/0191-8141(92)90053-Y
Hutchinson J. W. (1976) Bounds and self-consistent estimates for creep of polycrystalline materials. Proceedings of the Royal Society of London A 348, 101–127.
Holyoke, C.W., Kronenberg, A.K., 2010. Accurate differential stress measurement using the molten salt cell and solid salt assemblies in the Griggs apparatus with applications to strength, piezometers and rheology. Tectonophysics 494, 17–31. https://doi.org/10.1016/j.tecto.2010.08.001
Jaoul, O., Tullis, J., Kronenberg, A., 1984. The effect of varying water contents on the creep behavior of Heavitree quartzite. J. Geophys. Res.: Solid Earth 89, 4298–4312. https://doi.org/10.1029/JB089iB06p04298
Karato, S.I., 2008. Deformation of earth materials. An Introduction to the Rheology of Solid Earth, 463.
Kidder, S., Hirth, G., Avouac, J.P., Behr, W., 2016. The influence of stress history on the grain size and microstructure of experimentally deformed quartzite. J. Struct. Geol. 83, 194–206. https://doi.org/10.1016/j.jsg.2015.12.004
Koch, P.S., Christie, J.M., Ord, A., George, R.P., 1989. Effect of water on the rheology of experimentally deformed quartzite. J. Geophys. Res. 94, 31–32. https://doi.org/10.1029/jb094ib10p13975
Kohlstedt, D.L., Evans, B., Mackwell, S.J., 1995. Strength of the lithosphere: constraints imposed by laboratory experiments. J. Geophys. Res.: Solid Earth 100, 17587–17602
Kronenberg, A.K., Tullis, J., 1984. Flow strengths of quartz aggregates: grain size and pressure effects due to hydrolytic weakening. J. Geophys. Res.: Solid Earth 4281–4297. https://doi.org/10.1029/JB089iB06p04281@10.1002/(ISSN)2169-9356.CHEMDEF1
Kronenberg, A.K., Kirby, S.H., Aines, R.D., Rossman, G.R., 1986. Solubility and diffusional uptake of hydrogen in quartz at high water pressures: implications for hydrolytic weakening. J. Geophys. Res.: Solid Earth 91, 12723–12741. https://doi.org/10.1029/JB091iB12p12723
Kuiper, E.J.N., Weikusat, I., De Bresser, J.H.P., Jansen, D., Pennock, G.M., Drury, M.R., 2020. Using a composite flow law to model deformation in the NEEM deep ice core, Greenland-Part 1: The role of grain size and grain size distribution on deformation of the upper 2207 m. Cryosphere 14, 2429–2448. https://doi.org/10.5194/tc-14-2429-2020
Luan, F.C., Paterson, M.S., 1992. Preparation and deformation of synthetic aggregates of quartz. J. Geophys. Res.: Solid Earth 97, 301–320. https://doi.org/10.1029/91JB01748
Lu, L.X., Jiang, D., 2019. Quartz Flow Law Revisited: The Significance of Pressure Dependence of the Activation Enthalpy. J. Geophys. Res. Solid Earth 124, 241–256. https://doi.org/10.1029/2018JB016226
Lusk, A.D.J., Platt, J.P., Platt, J.A., 2021. Natural and Experimental Constraints on a Flow Law for Dislocation-Dominated Creep in Wet Quartz. J. Geophys. Res. Solid Earth 126, 1–25. https://doi.org/10.1029/2020JB021302
Manning, C.E., 1994. The solubility of quartz in H2O in the lower crust and upper mantle. Geochem. Cosmochim. Acta 58, 4831–4839. https://doi.org/10.1016/0016-7037(94)90214-3
Manning, C.E., 2018. Fluids of the deep crust: deep is different. Annu. Rev. Earth Planet Sci. 46, 67–97. https://doi.org/10.1146/annurev-earth-060614-105224
Nabarro, F. R. N. 1948. Deformation of crystals by the motion of single ions (pp. 75–90). Report of a Conference on the Strength of Solids. Bristol, UK

Nègre, L., Stünitz, H., Raimbourg, H., Lee, A., Précigout, J., Pongrac, P., Jeřábek, P., 2021. Effect of pressure on the deformation of quartz aggregates in the presence of H2O. J. Struct. Geol. 148. https://doi.org/10.1016/j.jsg.2021.104351
Paterson, M.S., Luan, F.C., 1990. Quartzite rheology under geological conditions. Geol. Soc. Lond. Spec. Publ. 54, 299–307. https://doi.org/10.1144/GSL.SP.1990.054.01.26
Paterson, M.S., 2012. Materials Science for Structural Geology. Springer Science & Business Media.
Pongrac, P., Jeřábek, P., Stünitz, H., Raimbourg, H., Heilbronner, R., Racek, M., Nègre, L., 2022. Mechanical properties and recrystallization of quartz in presence of H2O: Combination of cracking, subgrain rotation and dissolution-precipitation processes. Journal of Structural Geology, p.104630.
Post, A.D., Tullis, J., Yund, R.A., 1996. Effects of chemical environment on dislocation creep of quartzite. J. Geophys. Res.: Solid Earth 101, 22143–22155. https://doi.org/10.1029/96JB01926
Précigout, J., Stünitz, H., Pinquier, Y., Champallier, R., Schubnel, A., 2018. High-pressure, high-temperature deformation experiment using the new generation Griggs-type Apparatus. JoVE, e56841. https://doi.org/10.3791/56841
Richter, B., Stünitz, H., Heilbronner, R., 2018. The brittle-to-viscous transition in polycrystalline quartz : An experimental study. J. Struct. Geol. 114, 1–21. https://doi.org/10.1016/j.jsg.2018.06.005
Rutter, E.H., Brodie, K.H., 2004. Experimental intracrystalline plastic flow in hot-pressed synthetic quartzite prepared from Brazilian quartz crystals. J. Struct. Geol. 26, 259–270. https://doi.org/10.1016/S0191-8141(03)00096-8
Samae, V., Cordier, P., Demouchy, S., Bollinger, C., Gasc, J., Koizumi, S., Mussi, A., Schryvers, D., Idrissi, H., 2021. Stress-induced amorphization triggers deformation in the lithospheric mantle. Nature 591, 82–86. https://doi.org/10.1038/s41586-021-03238-3
Sassier, C., Leloup, P.H., Rubatto, D., Galland, O., Yue, Y., and Lin, D., 2009, Direct measurement of strain rates in ductile shear zones: A new method based on syntectonic dikes: Journal of Geophysical Research, v. 114, p. B01406, doi:10.1029/2008JB005597.
Scholz, C. (1998) Earthquakes and friction laws. Nature 391, 37-42.
Stipp, M., Stünitz, H., Heilbronner, R., Schmid, S.M., 2002a. The eastern Tonale fault zone: A "natural laboratory" for crystal plastic deformation of quartz over a temperature range from 250 to 700 °C. J. Struct. Geol. 24, 1861–1884. https://doi.org/10.1016/S0191-8141(02)00035-4
Stipp, M., Stünitz, H., Heilbronner, R., Schmid, S.M., 2002b. Dynamic recrystallization of quartz: Correlation between natural and experimental conditions. Geol. Soc. Spec. Publ. 200, 171–190. https://doi.org/10.1144/GSL.SP.2001.200.01.11
Stipp, M., Tullis, J., Behrens, H., 2006. Effect of water on the dislocation creep microstructure and flow stress of quartz and implications for the recrystallized grain size piezometer. J. Geophys. Res. Solid Earth 111, 1–19. https://doi.org/10.1029/2005JB003852
Stockli, D., Brichau, S., Dewane, T., 2006. Dynamics of large-magnitude extension in the Whipple Mountains metamorphic core complex. Geochim. Cosma Acta 70, A616.
Stünitz, H., Thust, A., Heilbronner, R., Behrens, H., Kilian, R., Tarantola, A., Fitz Gerald, J.D., 2017. Water redistribution in experimentally deformed natural milky quartz single crystals—Implications for H2O-weakening processes. J. Geophys. Res. Solid Earth 122, 866–894. https://doi.org/10.1002/2016JB013533
Tokle, L., Hirth, G., Behr, W.M., 2019. Flow laws and fabric transitions in wet quartzite. Earth Planet. Sci. Lett. 505, 152–161. https://doi.org/10.1016/j.epsl.2018.10.017
Yabe, K., Sueyoshi, K., Hiraga, T., 2020. Grain-Boundary Diffusion Creep of Olivine: 1. Experiments at 1 atm. J. Geophys. Res. Solid Earth 125, 1–33. https://doi.org/10.1029/2020JB019416

Fig. 1. Cross-polarized light-microphotograph of the representative undeformed Tana quartzite showing mosaic-like microstructure without any evidence of internal deformation like undulatory extinction.

Fig. 2. Mechanical data and the configuration of the experiment. a) Schematic diagram of the experimental set-up in the new generation Griggs-type deformation apparatus. b) A typical load-stepping mechanical force *versus* time curve to constrain the hit point. c) A typical stress-strain-time data obtained during stress-stepping experiment at 850°C, 1GPa (OR86). d) A typical stress-strain-time data obtained during temperature-steeping (900 to 750°C) at constant load (OR94).

Fig. 3. Determination of stress exponent (n) in a log-log space. Co-axial strain-rate-stepping experiments using the conventional Griggs apparatus are plotted as PP (Pongrac et al., submitted). a) Differential stresses and strain rates for all our experiments (H_2O-added and as-is ones) are plotted. The slope of the global fit indicates the n value. b) Only the H_2O-added experimental data are shown. Global-fit is calculated without considering the transparent data points in OR86 (green color) and OR89 (yellow color). c) Only the as-is experimental data are shown. Global-fit is calculated without considering the transparent data point in OR90 (blue color).

Fig. 4. Arrhenius plots of $\ln(\dot{\varepsilon})$ against inverse of temperature ($10000/T$) for both the H_2O-added (a) and as-is (b) Tana quartzite. The determination of the Q-value without previous knowledge of the n-value is a great advantage of the stress-stepping-tests. Our Q-value of 110 kJ/mol is the lowest Q-value determined so far from solid-medium piston-cylinder (Table 1). However, it is in the same range of values as the studies by Kronenberg and Tullis (1984) and Paterson and Luan (1990).

Fig. 5. Microstructural observations from deformed Tana quartzite under a light microscope (LM) and scanning electron microscope (SEM). a) SEM-CL-imaging of the undeformed Tana quartzite for comparison with the deformed samples. Individual quartz grains are composed of cores of rounded detrital quartz grains, surrounded by a dark luminescent crystalline authigenic silica cement. b, c) Under the LM, deformed H_2O-added samples show strong evidence of crystal-plastic deformation features, including undulatory to patchy extinction, deformation lamellae, grain boundary undulations, and subgrain formation. d-h) Compression direction is vertical. In the deformed sample, thin bright luminescence materials are formed along the cracks and boundaries of the quartz grain. Yellow arrows indicate mode-I cracks, while the green arrow indicate unloading cracks. These cracks are healed by silica during the deformation. Such places are associated with porosity generation, as shown in the secondary electron image, marked by a white circle (e). Red arrows show cracked grains, which are formed along the grain boundaries and within the dark cement material. Blue arrows indicate features similar to grain boundary migration (GBM). A careful inspection reveals that these wavy grain boundaries are marked by thin white luminescent material, which indicates the mobility of grain boundaries.

Fig. 6. Corresponding CL and EBSD images from the deformed as-is sample (OR90). The compression direction is horizontal. We plot the following three types of boundaries in our EBSD maps: i) high-angle grain boundaries (black lines) defined by misorientation angle >10°, ii) low-angle boundaries defined by misorientations between 2 to 10° and including sub-grain boundaries (red lines) and inner boundaries (yellow lines). While sub-grain boundaries form closed polygons, the yellow inner boundaries do not. a) The yellow box on the CL image indicates the location of the EBSD mapping**.** b) Misorientation analysis reveals a high degree of internal ("mis2mean" function in MTEX) crystal plastic deformation in the original quartz grain. c) Individual grains are drawn based on their crystallographic orientation with respect to the compression direction (~ East). Crystallographic orientations of grains relative to each other are given by the inverse pole figure scheme. d) The location of the CL image is marked by a black rectangle in the previous figures. The fine-grained materials at the junction of the four original grains might have been identified as the product of dynamic recrystallization. However, the corresponding CL image reveals that this fine-

grained material has developed due to cracking in the cement. e) Misorientation axes distribution of low-angle boundaries indicate dominant prism <a> slip with minor rhomb <a> contribution.

Fig. 7. Comparisons of our newly developed dislocation creep law for wet quartzite with the results of previous studies in nondimensional and semi-nondimensional spaces. To make a rational comparison with our experimental condition, we only included the results from studies that were conducted in a coaxial geometry at ≥750°C, and satisfying the Goetze criterion. a) Plot of nondimensionalized strain rate ($\dot{\varepsilon}_0$) as a function of nondimensionalized stress (σ_0), calculated from the original mechanical data (σ and $\dot{\varepsilon}$) as reported in the previous literature. b) Nondimensionalized strain rate ($\dot{\varepsilon}_0$) as a function of inverse temperature (T_0^{-1}). Acronyms used in these plots are as follows. K&T84: Kronenberg and Tullis, (1984); Koch 89: Koch et al.,(1989); L&P92: Luan and Paterson, (1992); Post 96: Post et al., (1996); G&T 95: Gleason and Tullis, (1995); H&T 02: Heilbronner and Tullis, (2002); S&T03: Stipp and Tullis, (2003); R&B04: Rutter and Brodie, (2004); Stipp 06: Stipp et al., (2006); Cher 09: Chernak et al., (2009); Kid 16: Kidder et al., (2016); Fukuda 18: Fukuda et al., (2018); Nègre: Nègre et al., (2021).

Fig. 8. A comparison between stress *versus* depth profile (assuming the average density of the crust as 2700 kg/m^3 and a geotherm of 30 °C/km). Our flow law predicts lower strength than popular flow laws at $\dot{\varepsilon} = 10^{-12}\,s^{-1}$. A strength variation at geologically viable strain rates is shown using our flow law. Yield stress envelopes are drawn based on the Byerlee's law (Byerlee, 1978).

Figure 1

Click here to access/download;Figure;Fig. 1..tiff

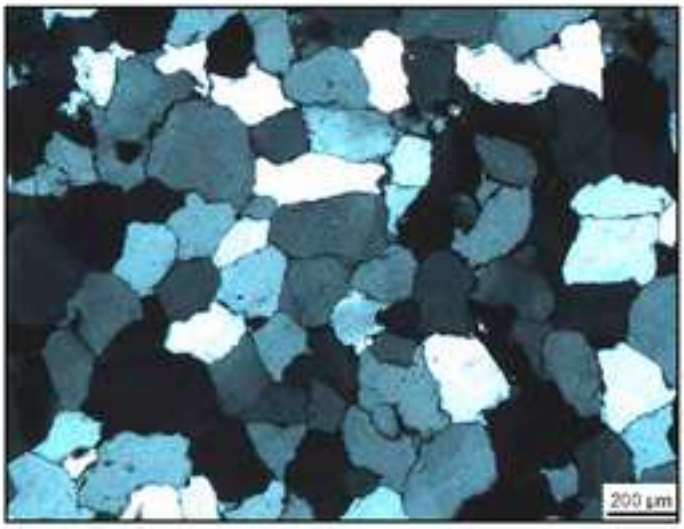

Figure 2

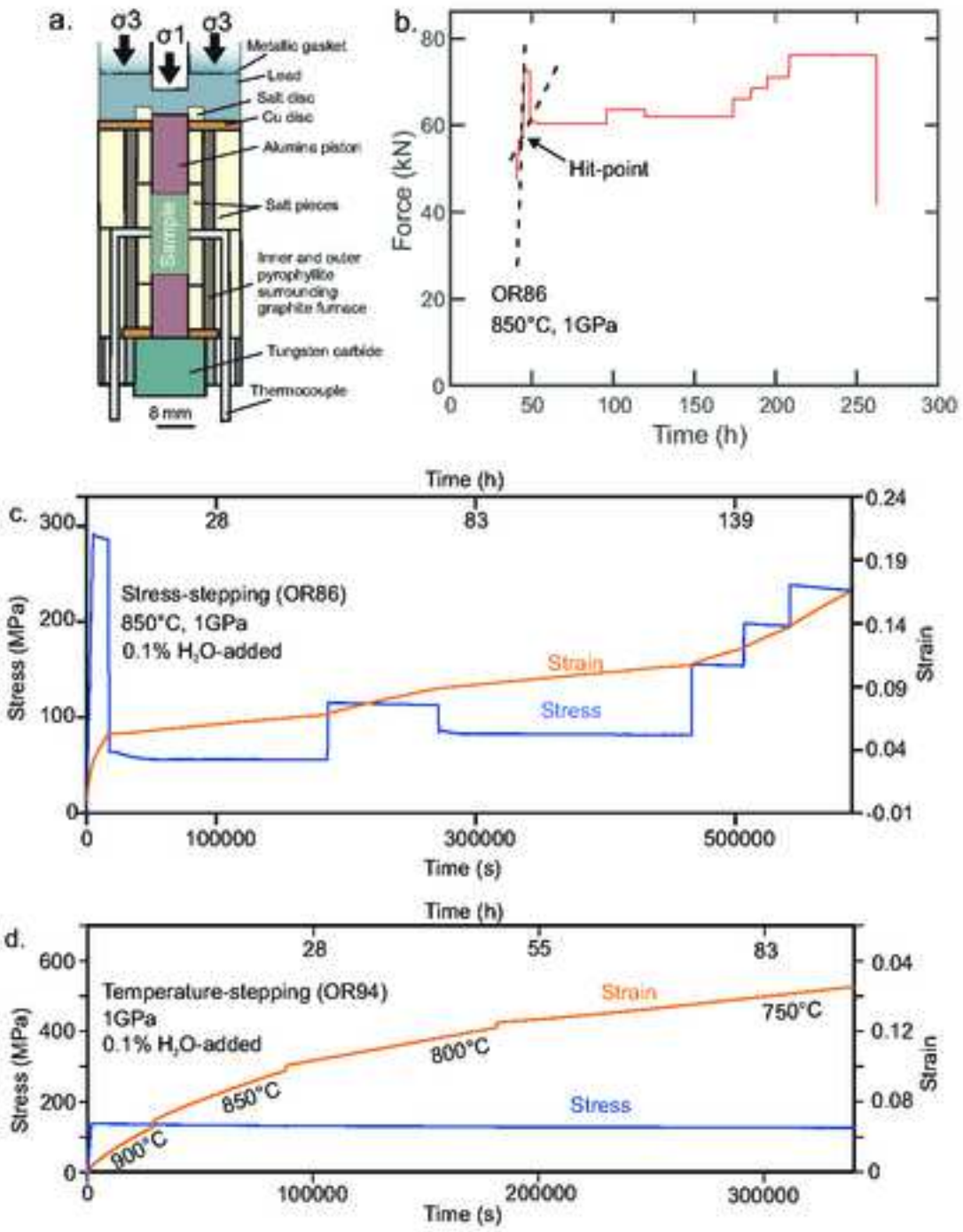

Figure 3

Click here to access/download;Figure;Fig. 3.pdf

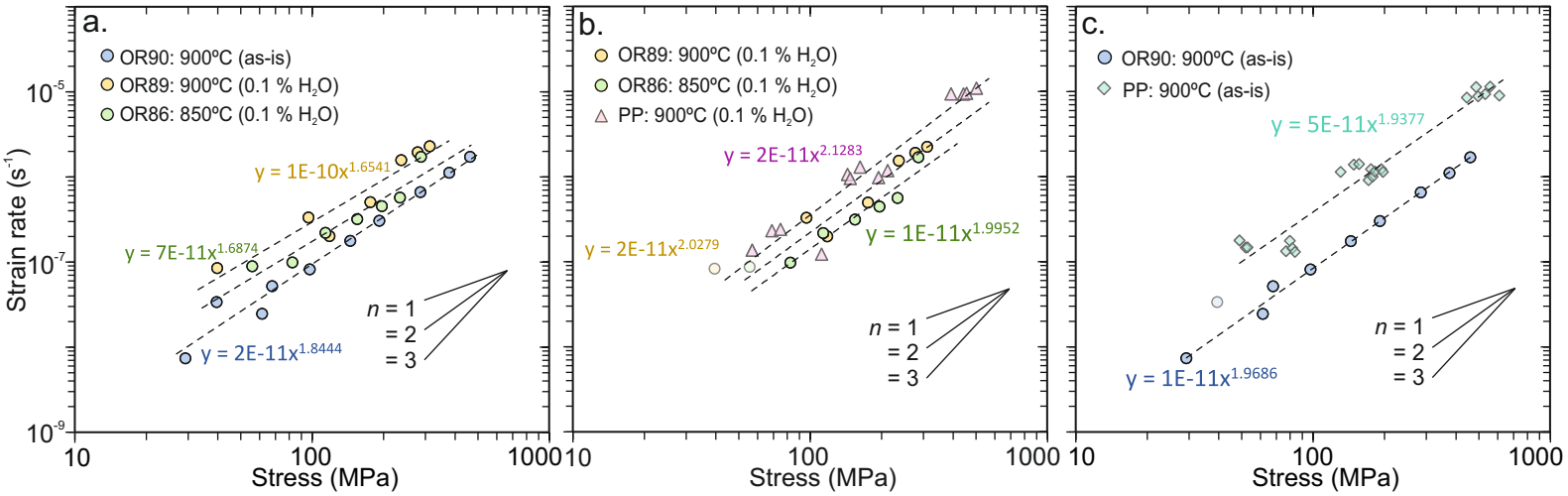

Figure 4

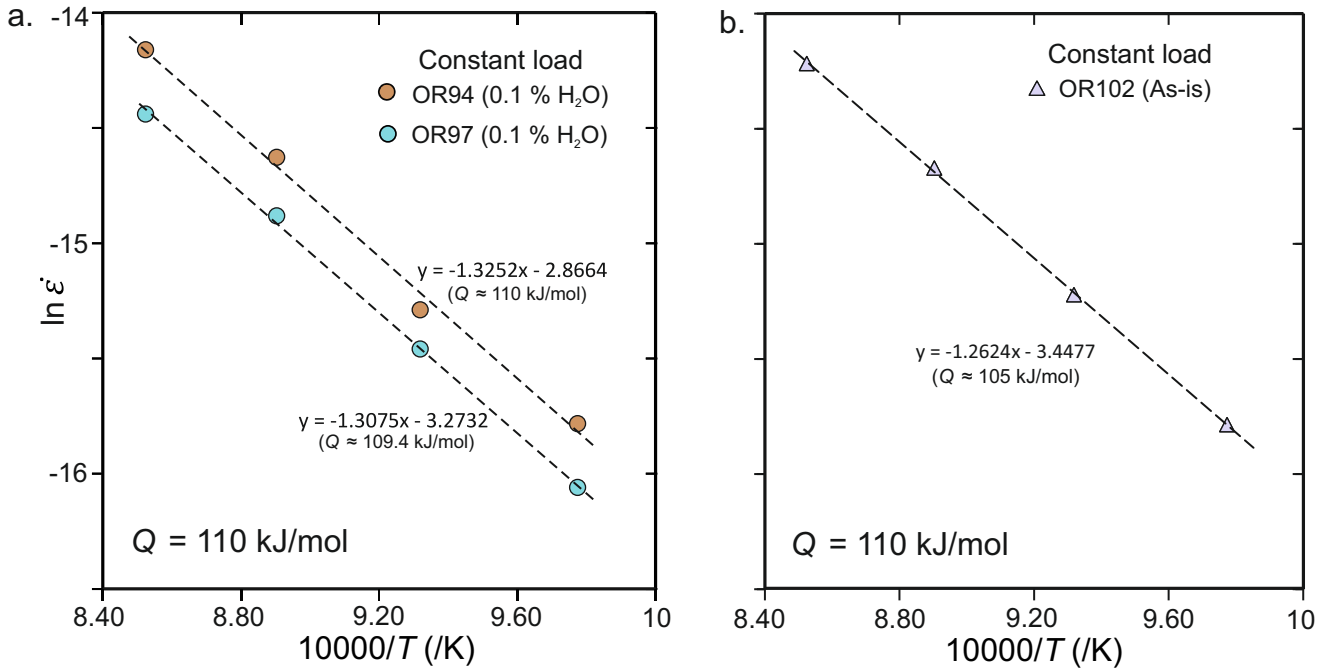

Figure 5

Click here to access/download;Figure;Fig. 5.pdf

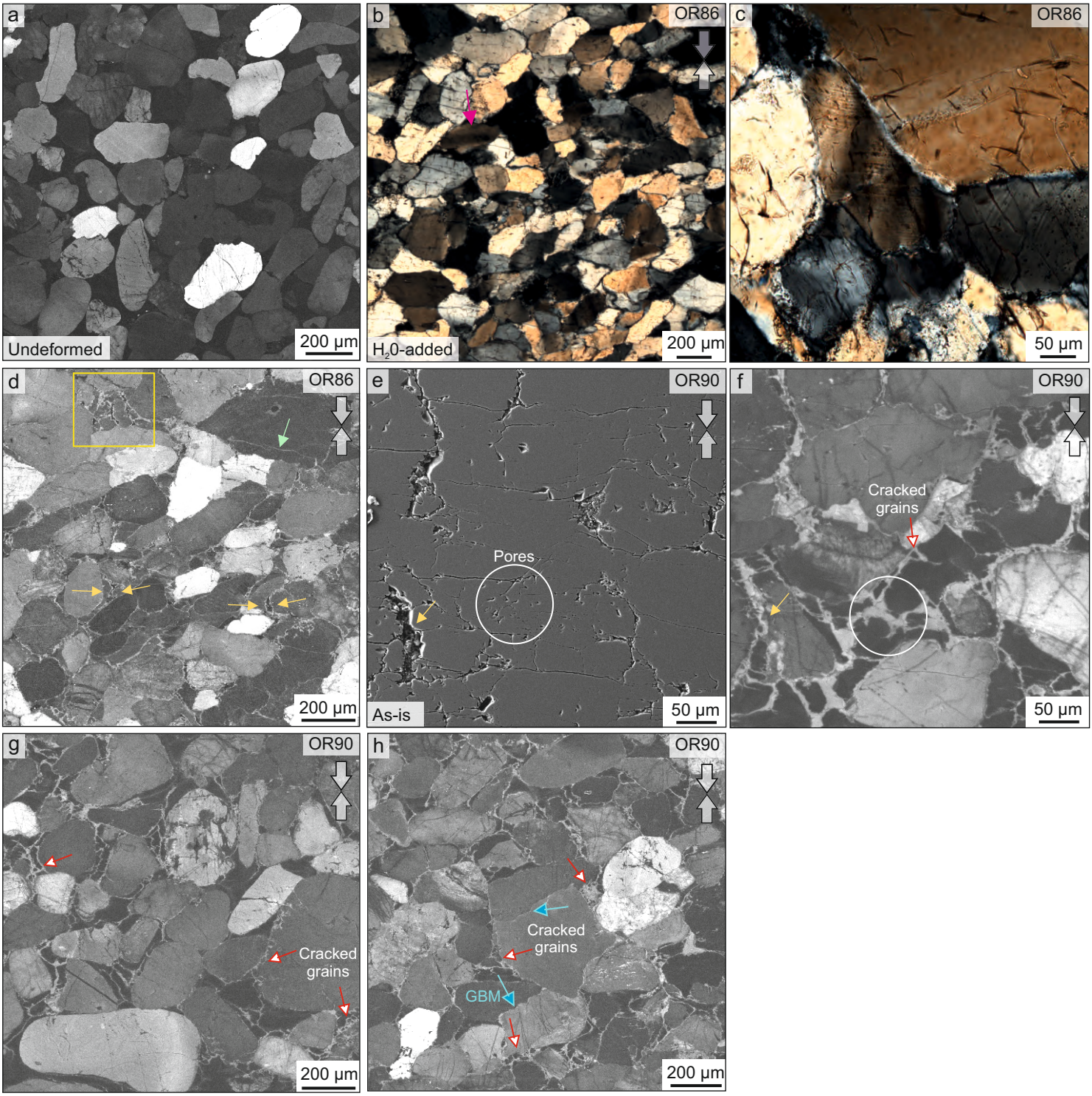

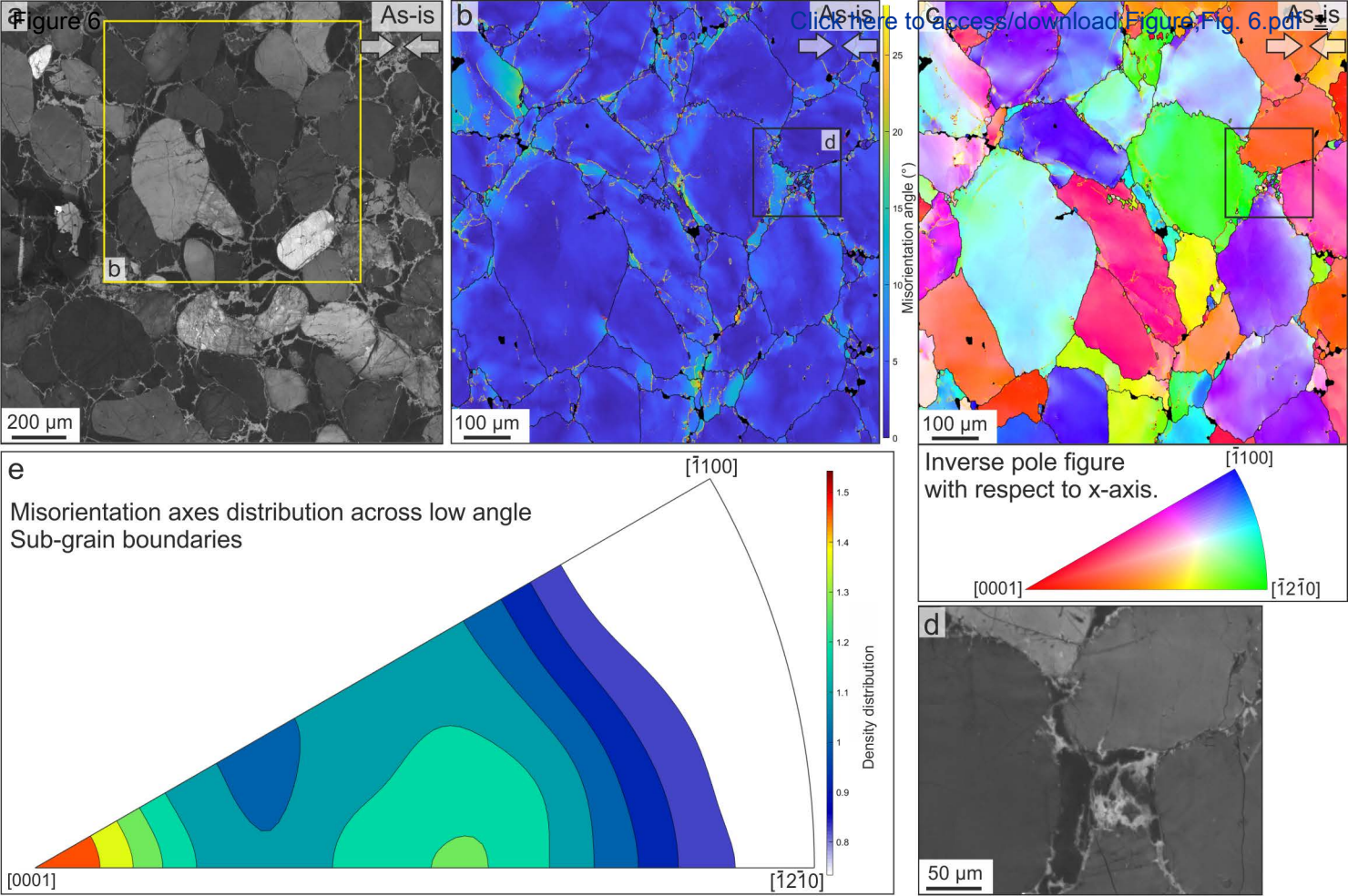

Figure 7

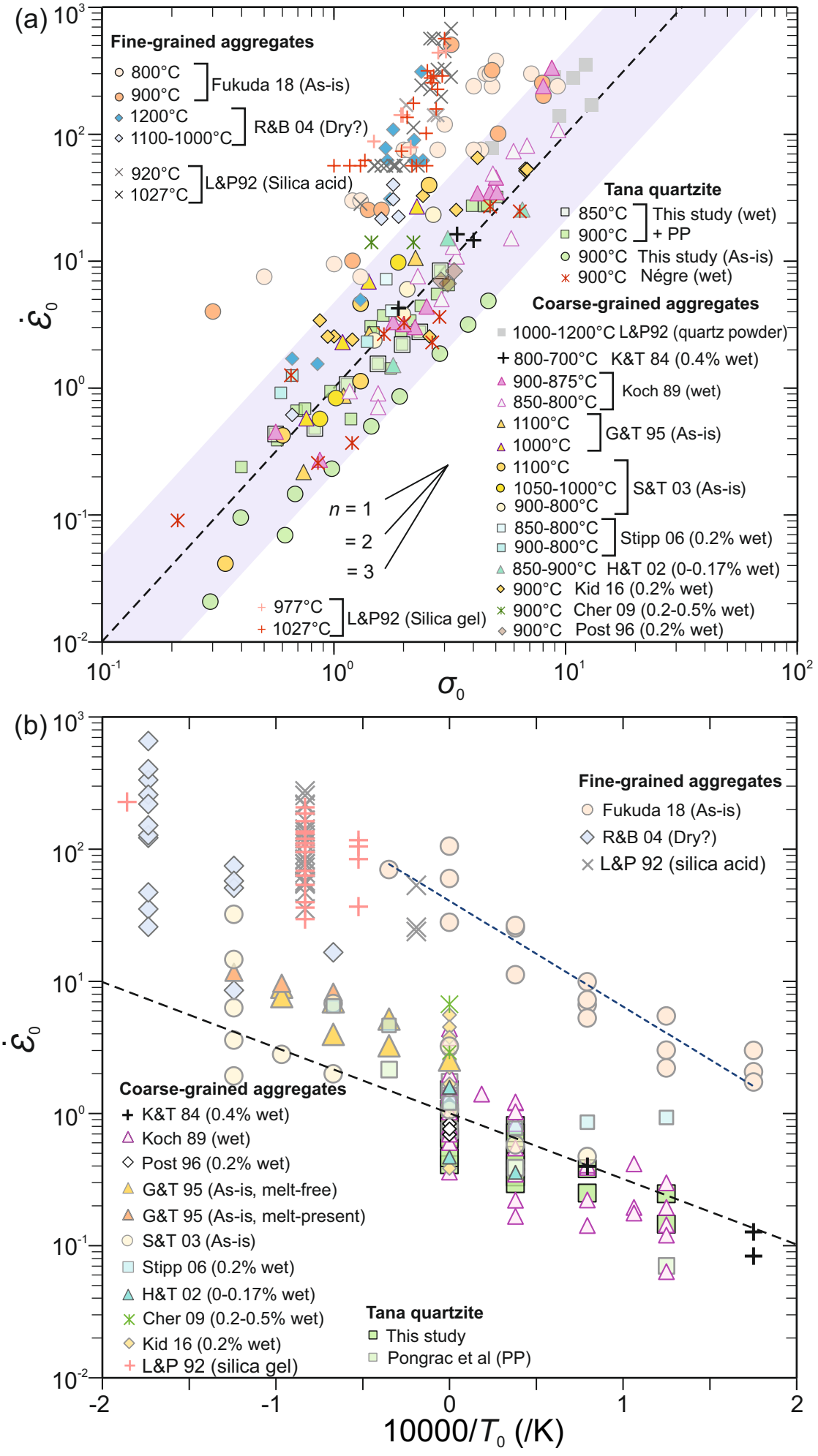

Figure 8

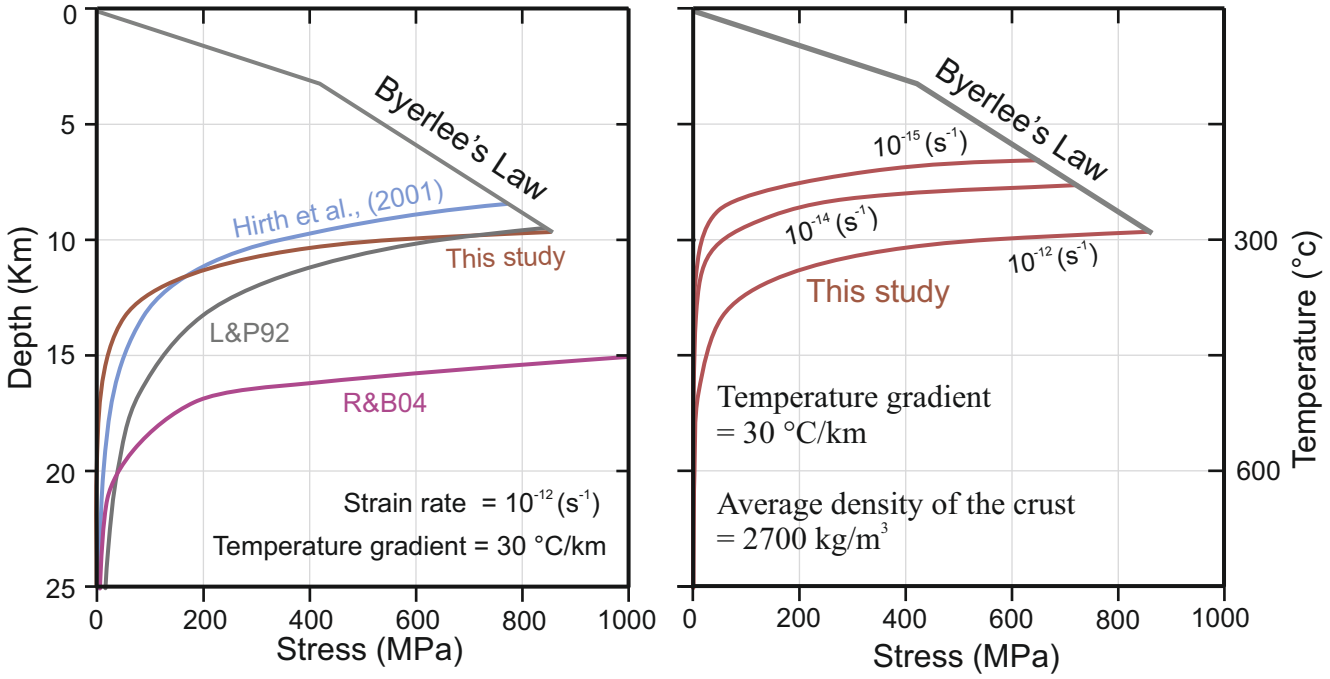

Table 1: Previously determined flow law parameters and the experimental conditions (also see Table S1).

Source	Experiment apparatus	Sample characterization	Deformation condition (T °C and P_c GPa)	Initial grain size (μm)	A (MPa^{-n} s^{-1})	Activation energy Q (kJ mol^{-1})	Stress exponent n	Grain size exponent p	Water fugacity exponent m
Kronenberg and Tullis (1984)	Solid salt medium	Heavitree quartzite: As-is (4000 – 5000 H/10^6 Si ≈ 0.05 wt. %).	650 to 1200; 0.90 to 1.17	211	–	170 – 220	2.9 – 3.2	–	–
	Solid salt medium	Heavitree quartzite: 0.4 wt.% water added.	600 to 900; 1.53 to 1.6	211	–	120 ± 10	2.7 ± 0.3	0.18	–
	Solid salt medium	Heavitree quartzite: vacuum dried at 1000-800 °C for 12 hrs.	919 to 1119; 0.95-1.45	211	–	300	4		–
	Solid salt medium	Arkansans novaculite: As-is.	1019 to 1269; 1.45	1.2	–	210 ± 10	–		–
	Solid salt medium	Arkansans novaculite: 0.4 wt.% water added.	600 to 950; 0.89 to 1.60	3.6 – 4.9	–	120 – 150	2.5 ± 0.07	0.18	–
Jaoul et al. (1984)	Solid salt medium	Heavitree quartzite: As-is	900 to 650, 1.5	211	3.11×10^{-4}	171 ± 8 (CaCO3)	2.3 ± 0.1	–	–
	Solid salt medium	Heavitree quartzite: 0.39 wt.% water added.	800, 1.5	211	2.91×10^{-3}	150.6	1.8 ± 0.2	–	–
	Solid salt medium	Heavitree quartzite: vacuum dried at 1010 °C for 5.5 hrs.	890, 1.5	211	–	–	3.3 ± 0.4 (CaCO 3)	–	–
Koch et al. (1989)	Solid dehydrated talc	Simpson quartzite: As-is (642 ± 47 H /10^6 Si ≈ 0.009 wt. %).	750 to 900; 1 to 1.25	210	1.16×10^{-7}	134 ± 32	2.72 ± 0.19	–	–
	Solid hydrated talc	Simpson quartzite: H_2O from wet talc.	750 to 900; 1 to 1.25	210	5.05×10^{-6}	145 ± 17	2.61 ± 0.15	–	–
Paterson and Luan (1990)	–	_	–	–	6.5×10^{-8}	135	3	–	–
Luan and Paterson (1992)	Gas medium	Silica acid (relatively pure): less than 0.4 wt.% water.	827 to 1027; 0.3	20 (~10 – 30)	4.0×10^{-10} (Modified to $\mathbf{10^{-7.20 \pm 0.52}}$)	152 ± 71 (Modified to **121 ± 13**)	4 ± 0.8 (Modified to **3**)	–	–
	Gas medium	Silica gel (impure): at least 0.1 – 0.2 wt.% water.	977 to 1027; 0.3	90 (30 – 95)	–	150	2.3 ± 03 (2.01 – 2.6)	–	–
Gleason and Tullis (1995)	Molten salt medium	Black Hills quartzite: **As-is** (~ 0.15 wt. %).	900 to 1100; ~1.5 to 1.7	100	1.1×10^{-4}	223 ± 56	4 ± 0.9 (Modified to **3.6**)	–	–
Hirth et al., (2001)	–	Previous Experiment + natural observation	–	–	6.3×10^{-12}	135 ± 14	4	–	1
Post et al. (1996)	Solid salt medium	Black Hills quartzite: 0.2 - 0.1 wt. % added.	900; 0.7 to 1.7	100	–	–	–	–	> 2 (using n = 3.9)
Rutter and Brodie (2004)	Gas medium	Crushed Brazilian single crystal quartz: low water content (~10 to 20 H/10^6Si).	1000 to 1200; 0.3	12 – 20	1.2×10^{-5}	242 ± 24	2.97 ± 0.29	–	–
Fukuda et al., (2018)	Solid salt medium	Natural quartz powder: 3,500 ppm H/Si ≈ 0.25 wt. % of adsorbed water.	600 to 750; 1.50	9.5 – 12	-	129 ± 33	2.9 to 5.2	–	1.0 ± 0.2
	Solid salt medium		800 to 950; 1.50	9.5 – 12	$1.0 \times 10^{-2.97}$	183 ± 25	1.7 ± 0.2	0.51 ± 0.13	1.0 ± 0.2
Richter et al. (2018)	Non-coaxial Solid salt medium	Crushed Alpine cleft quartz: 0.2 wt.% H_2O added.	800 to 1000; 1.5	< 100	3.1×10^{-4}	~ 170	1.8 – 2	~1.08	–
Nègre et al., (2021)	Solid salt medium	Tana quartzite: 0.1 wt. % added.	900; 0.6 to 2	~ 200	–	–	~ 2	–	~ 1

Table 2a. Experimental results of stepped load tests.

Experiment no.	T (°C)	P_c (GPa)	H_2O (%)	H (mm)	σ (MPa)	$\dot{\varepsilon}$ (s^{-1})	Final ε (%)
OR86	850	1	0.1	14.86	287.28	1.73E-06	~ 16.60
					55.90	8.94E-08	
					113.76	2.20E-07	
					82.63	9.89E-08	
					154.84	3.19E-07	
					196.77	4.53E-07	
					234.40	5.71E-07	
OR89	900	1	0.1	14.64	96.56	3.34E-07	~ 15
					39.83	8.47E-08	
					237.28	1.57E-06	
					278.59	1.95E-06	
					312.75	2.29E-06	
					118.26	2.02E-07	
					175.83	5.06E-07	
OR90	900	1	as-is	14.91	39.59	3.39E-08	~ 6.6
					67.89	5.20E-08	
					97.71	8.21E-08	
					144.84	1.77E-07	
					61.50	2.46E-08	
					29.22	7.40E-09	
					191.98	3.05E-07	
					285.85	6.63E-07	
					378.39	1.12E-06	
					462.91	1.72E-06	

Table 2b. Experimental results of stepped heating in constant-load tests.

Experiment no.	T (°C)	P_c (GPa)	H_2O (%)	H (mm)	σ (MPa)	$\dot{\varepsilon}$ (s^{-1})	Final ε (%)
OR94	900	1	0.1	15.02	136.32	7.08E-07	~ 10.50
	850				132.77	4.44E-07	
	800				130.34	2.29E-07	
	750				126.67	1.40E-07	
OR97	900	1	0.1	15.04	153.51	5.36E-07	~ 9.80
	850				150.21	3.44E-07	
	800				147.86	1.93E-07	
	750				143.80	1.06E-07	
OR102	900	1	as-is	15.04	146.48	6.69E-07	~ 10.25
	850				142.71	4.25E-07	
	800				139.21	2.45E-07	
	750				135.76	1.39E-07	

Table 3**:** Strain rates calculated from natural shear zones (also see Table S2).

Source	Grain size (μm)	σ (MPa)	T (°C)	P_c (MPa)	$\dot{\varepsilon}$ (This study) (s^{-1})	$\dot{\varepsilon}$ (Hirth) (s^{-1})	$\dot{\varepsilon}$ (R&B) (s^{-1})	$\dot{\varepsilon}$ (L&P) (s^{-1})
Stipp et al., (2002b)								
BLG								
27-3	5.5	173.31	304.8	300	1.40E-13	9.36E-14	1.84E-19	6.59E-15
27-1	7.8	131.34	318.4	300	1.56E-13	6.74E-14	2.94E-19	4.50E-15
26-2	8.7	120.43	345.6	300	4.56E-13	2.07E-13	2.57E-18	1.24E-14
25-3	14.3	81.18	369.4	300	5.52E-13	1.36E-13	5.49E-18	7.64E-15
25-1	15.5	76.15	383	300	8.39E-13	2.01E-13	1.31E-17	1.07E-14
24-4	24.3	53.30	400	300	7.61E-13	1.00E-13	1.55E-17	5.17E-15
SGR								
13-1	58	26.72	451	300	1.06E-12	4.81E-14	5.82E-17	2.21E-15
23-1	61	25.67	461.2	300	1.34E-12	5.94E-14	9.58E-17	2.68E-15
14-5	74	22.02	495.2	300	2.59E-12	1.01E-13	4.16E-16	4.36E-15
15-2	84	19.91	515.6	300	3.63E-12	1.28E-13	9.01E-16	5.40E-15
GBM								
21-2	219	9.31	560	300	2.31E-12	2.19E-14	8.03E-16	8.86E-16
16-3	354	6.36	563	300	1.16E-12	5.19E-15	2.98E-16	2.09E-16
Boutonnet et al., (2013)								
SGR								
YY33	62	25.34	425 ± 40	130± 80	2.10E-13	7.32E-15	4.83E-18	6.99E-16
YY35	58	26.72	425 ± 40	130± 80	2.33E-13	9.05E-15	5.65E-18	8.64E-16
Bher and Platt, (2011)								
PW77	135	13.66	544	560	8.10E-12	1.54E-13	2.81E-15	2.68E-15
PW4	73	22.26	500	480	5.58E-12	2.28E-13	1.03E-15	5.28E-15
PW5	53	28.70	500	480	9.27E-12	6.31E-13	2.19E-15	1.46E-14
PW25	80	20.70	500	480	4.82E-12	1.71E-13	8.28E-16	3.95E-15
PW101	75	21.79	478	430	2.49E-12	8.71E-14	2.46E-16	2.42E-15
PW104Q	68	23.55	475	430	2.71E-12	1.09E-13	2.66E-16	3.00E-15
PW44	43	33.88	405	340	4.28E-13	2.35E-14	6.68E-18	1.03E-15
PW87	52	29.14	416	360	5.05E-13	2.21E-14	9.89E-18	8.68E-16
PW75b	33	41.80	406	340	6.80E-13	5.73E-14	1.35E-17	2.49E-15
PW80b	18	67.63	406	340	1.78E-12	3.92E-13	5.62E-17	1.70E-14
PW34b	24	53.82	387	320	5.18E-13	6.37E-14	6.69E-18	3.15E-15
PW24b	36	39.01	376	310	1.74E-13	1.04E-14	1.09E-18	5.44E-16
PW79b	16	74.26	350	280	1.91E-13	3.42E-14	8.10E-19	2.20E-15
PW24a	11	99.98	357	290	4.87E-13	1.66E-13	3.65E-18	1.00E-14
PW34a	7	143.12	308	240	8.70E-14	4.07E-14	1.10E-19	3.65E-15
PW75a	8	128.73	308	240	7.04E-14	2.67E-14	8.05E-20	2.39E-15
PW79a	6	161.74	331	260	3.65E-13	2.66E-13	1.47E-18	1.97E-14
PW80a	5	186.93	308	240	1.48E-13	1.19E-13	2.44E-19	1.06E-14